Supplementary Information (SI) for Chemical Science.

Supporting Information

Molten-Salt Flash Synthesis of P-Doped Iron Oxide with Engineered Oxygen Vacancies for Lattice-Oxygen Water Oxidation

Jiahui Luo[a,b], Baoxin Wu[a,c], Kejun Yan[a,b], Yongbiao Mu[a,b], Qing Zhang[a,b], Huanxiu Zou[d], Zhiqing Tang[a.b], Guobin Zhang[e], Wanwisa Limphirat[f], Wenjia Li [a,b], Lin Zeng [a,b]**

[a] Department of Mechanical and Energy Engineering, Southern University of Science and Technology, Shenzhen 518055, China.

[b] SUSTech Energy Institute for Carbon Neutrality, Southern University of Science and Technology, Shenzhen 518055, P. R. China.

[c] Department of Mechanical Engineering, The Hong Kong Polytechnic University, Hung Hom, Kowloon, Hong Kong SAR, P. R. China.

[d] Key Laboratory of Hunan Province for Advanced Carbon-based Functional Materials, School of Chemistry and Chemical Engineering, Hunan Institute of Science and Technology, Yueyang 414006, P R. China.

[e] Future Technology School, Shenzhen Technology University, Shenzhen, 518118 China.

[f] Synchrotron Light Research Institute, 111 University Avenue, Muang District, Nakhon Ratchasima 30000, Thailand.

**Corresponding author.*

liwj@sustech.edu.cn;

zengl3@sustech.edu.cn;

1. Characterizations

The powder X-ray diffraction (XRD) patterns were obtained by an X-ray diffractometer (XRD, Bruker Advance D8) with Cu Kα radiation (λ= 1.5406 nm). The morphologies of catalysts were observed by scanning electron microscope (SEM, Sigma 300). The microstructure and elemental mapping were performed using a Talos instrument (F200X G2, voltage of 300 kV). Raman spectra (Raman, LabRAM HR Evolution) was obtained at the wavelength of 532 cm^{-1}. X-ray photoelectron spectra (XPS, Escalab 250Xi) was collected on a Thermo SCIENTIFIC ESCALAB 250Xi with Al kαhv = 1486.8 eV) as the excitation source.

2. Electrochemical Measurements

All electrochemical tests were conducted on a IVIUMnSTAT workstation using a standard three electrode system, with as-obtained catalyst serving as the working electrode, a graphite rod used as the counter electrode, and the Hg/HgO electrode as the reference electrode. Before experiment, we thoroughly rinsed the cells with deionized water and prepared 1 M alkaline electrolyte to prevent contamination. The preparation of the working electrode could be summarized as follows: First, the catalyst ink was prepared by dispersing 5 mg catalyst into 0.5 mL solution containing 0.01 mL of Nafion (5 wt.%) and 0.49 mL of ethanol. Then, the mixture was ultrasonically treated for 60 minutes to obtain a uniform catalyst ink. Next, catalyst ink was dropped onto the Ni foam (1*1 cm^2) with the loading of 1 mg cm^{-2} and allowed the droplets to air dry under the light. Linear sweep voltammetry (LSV) measurements were performed in alkaline electrolytes using a scan rate of 2 mV s^{-1} after catalyst activation. SCE was converted to a reverse hydrogen electrode (RHE) according to the equation $E_{RHE} = E_{SCE} + E_{REF}$. The overpotentials of OER were obtained according to the equation $\eta = E_{RHE} - 1.23$ V. Electrochemical impedance spectroscopy (EIS) was recorded from 0.1 Hz to 100 kHz, applying 5 mV perturbation at 1.53 V vs. RHE. Scan-rate-dependent cyclic voltammetry, performed in a Faradaic-silent potential window, supplied the double-layer capacitance (C_{dl}) values, which in turn were used to calculate the electrochemically active surface area (ECSA) for each sample. Long-term stability was subsequently assessed with a potentiostatic test following an accelerated degradation protocol of 18,000 cycles at 100 mV s^{-1}. E-t tests were conducted at 100 mA cm^{-2} over 2000 h.

3. AEM water electrolyzer

To evaluate the practical applicability of the catalysts in an AEM water electrolyzer, a full-cell device was assembled using Pt/C as the cathode and P/FeOx as the anode. Commercial Pt/C catalyst (20 % Pt on carbon black, Accelerate® PT-A) was spray-coated onto carbon paper with a total Pt/C loading of 0.5 mg cm^{-2}. The synthesized P/FeOx catalyst ink was drop-cast onto Ni foam and dried under ambient conditions to achieve an anode catalyst loading of 1.0 mg cm^{-2}. Prior to assembly, the anion-exchange membrane with a geometric area of 1.5 × 1.5 cm^2 was soaked in 1.0 M KOH for 24 h. The active electrode area of electrolyzer was1 cm^2. Polarization curves for the AEM single-cell were measured at a scan rate of 2 mV s^{-1} using a Biologic workstation (without iR compensation). System stability was assessed under constant current (500 mA cm^{-2} at 60°C) via a Neware electrochemical station.

Computational Details and Models

Spin-polarized DFT calculations were conducted through the Vienna ab initio Simulation Package (VASP) with the projector augment wave method. Generalized gradient approximation of the Perdew-Burke-Ernzerhof (PBE) functional was used as the exchange-correlation functional. To account for the strong on-site Coulomb interaction of Fe 3d electrons, DFT+U calculations were performed for Fe-containing systems. An effective Hubbard parameter of Ueff = 6.3 eV was applied to the Fe 3d orbitals. This value was adopted from the benchmark study by Bennett et al., in which Ueff = 6.3 eV was systematically determined for α-Fe_2O_3 by comparing the calculated band gap, magnetic moment, and antiferromagnetic ground-state stability with experimental results. Therefore, this value was used in the present work to provide a reasonable description of hematite-type FeOx. The Brillouin zone was sampled with 2 × 2 × 1 K points for surface calculation. The cutoff energy was set as 500 eV, and structure relaxation was performed until the convergence criteria of energy and force reached 1×10^{-5} eV and 0.02 eV $Å^{-1}$, respectively. A vacuum layer of 15 Å was constructed to eliminate interactions between periodic structures of surface models. The van der Waals (vdW) interaction was amended by the zero damping DFT-D3 method of Grimme.

The vacancy formation energy (ΔE_{vac}) was calculated as:

$$\Delta E_{vac} = E_{defect} - E_{perfect} + \mu_O$$

where E_{defect} is the total energy of the system with the vacancy, $E_{perfect}$ is the total energy of the pristine system, and μ_O is the chemical potential of the removed atom O in its reference state.

The Gibbs free energy was calculated as $\Delta G = \Delta E + \Delta E_{ZPE} - T\Delta S + \Delta G_U + \Delta G_{pH}$, where the ΔE, ΔE_{ZPE}, and ΔS are electronic energy, zero-point energy, and entropy difference between products and reactants. $\Delta G_U = -eU$, where e is the elementary charge, U is the electrode potential, ΔG_{pH} is the correction of the H^+ free energy. The zero-point energies of isolated and absorbed intermediate products were calculated from the frequency analysis. The vibrational frequencies and entropies of molecules in the gas phase were obtained from the National Institute of Standards and Technology (NIST) database.

4. Supporting Figures

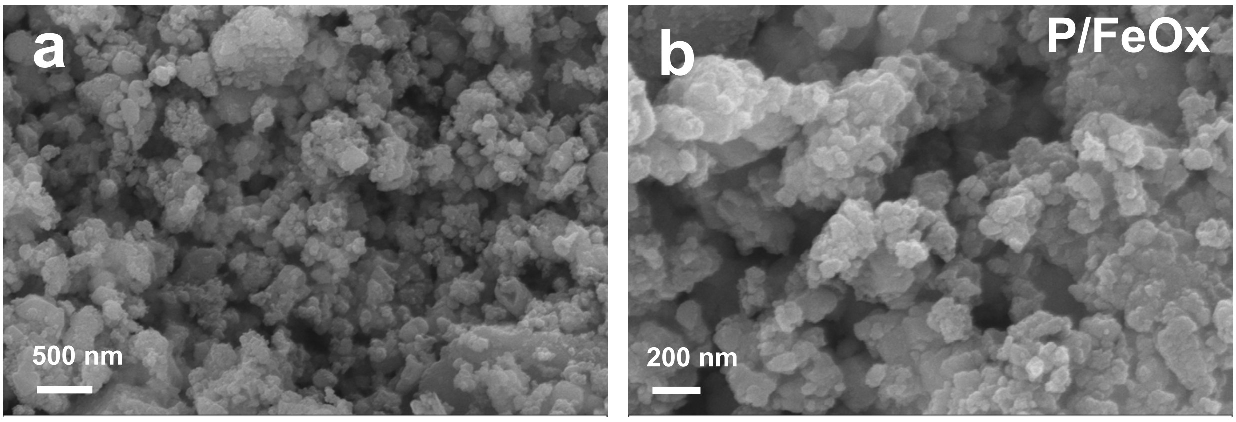

Figure S1. SEM image for the P/FeOx.

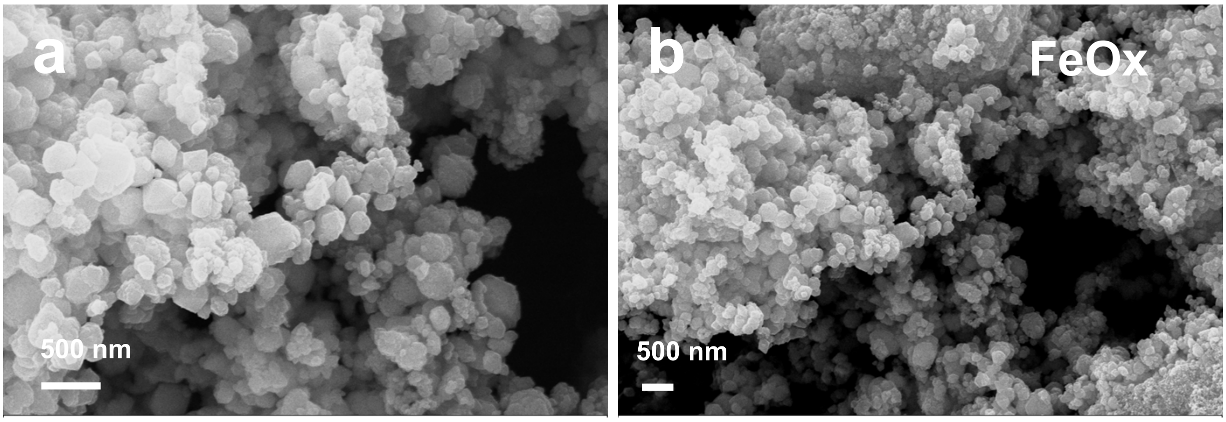

Figure S2. SEM image for the FeOx.

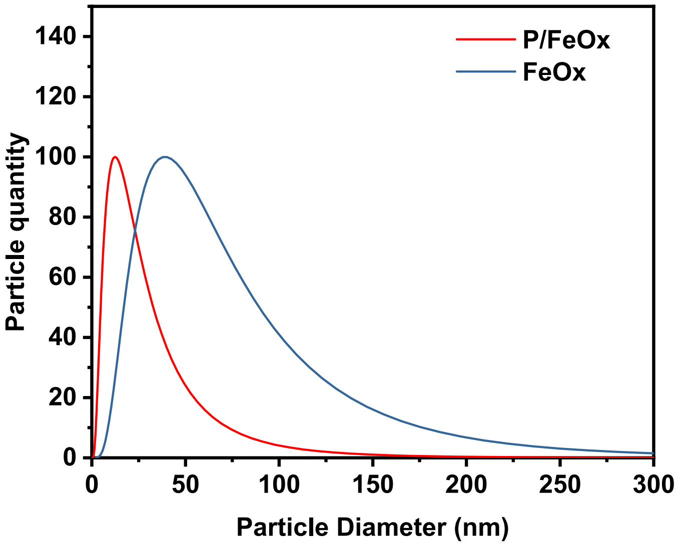

Figure S3. Particle size distribution map of catalysts measured by particle size analyzer.

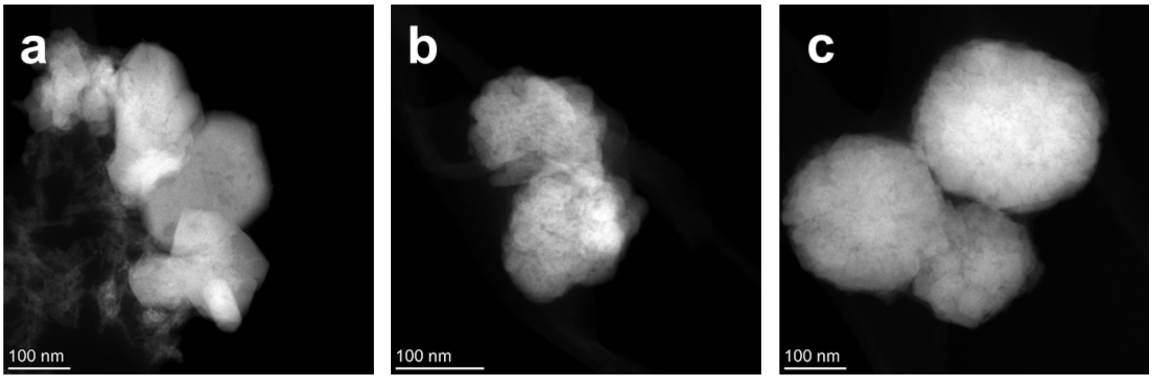

Figure S4. STEM images for P/FeOx catalyst.

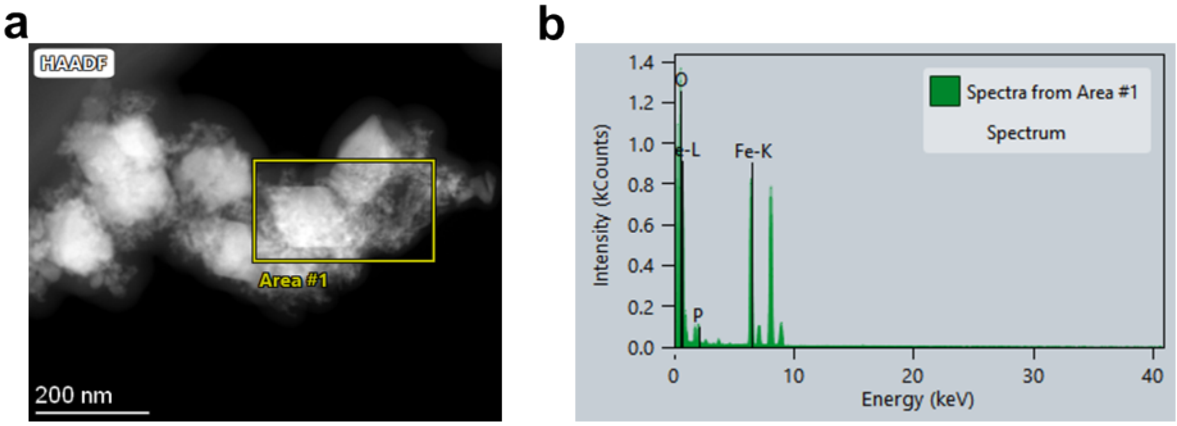

Figure S5. (a) HAADF image and (b) its element distribution spectra from Area #1 for P/FeOx catalyst.

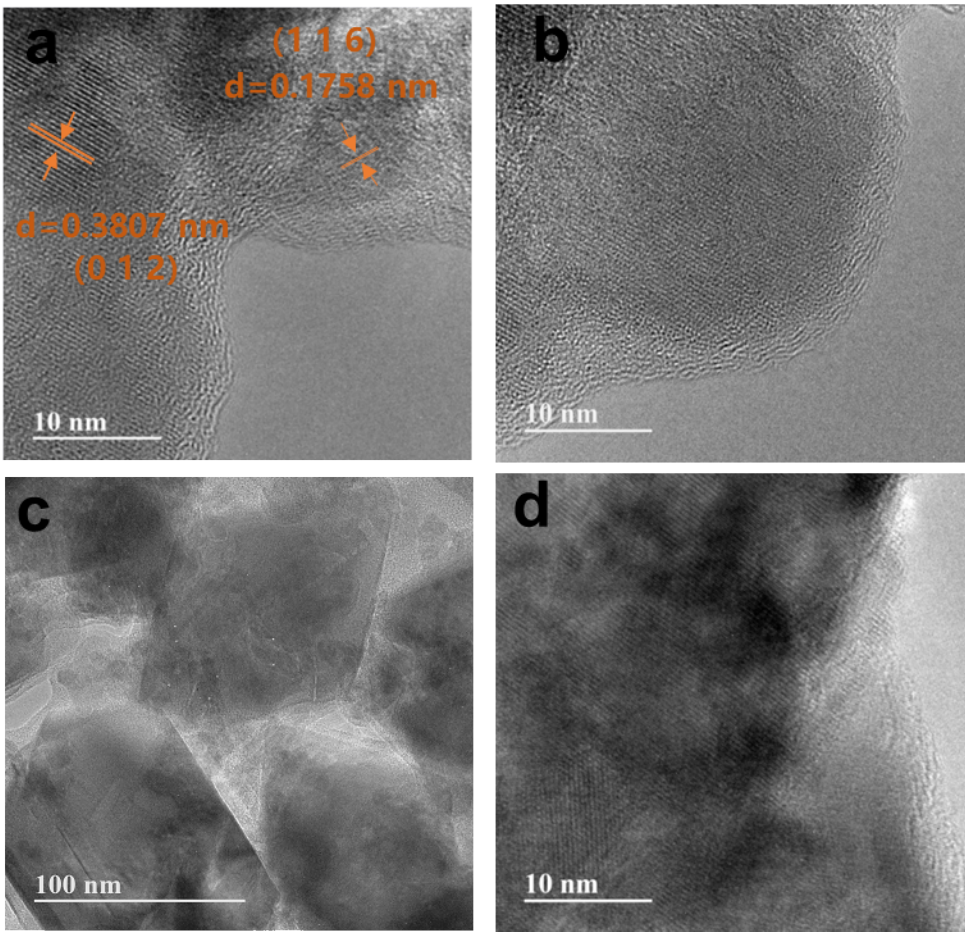

Figure S6. TEM images for P/FeOx catalyst.

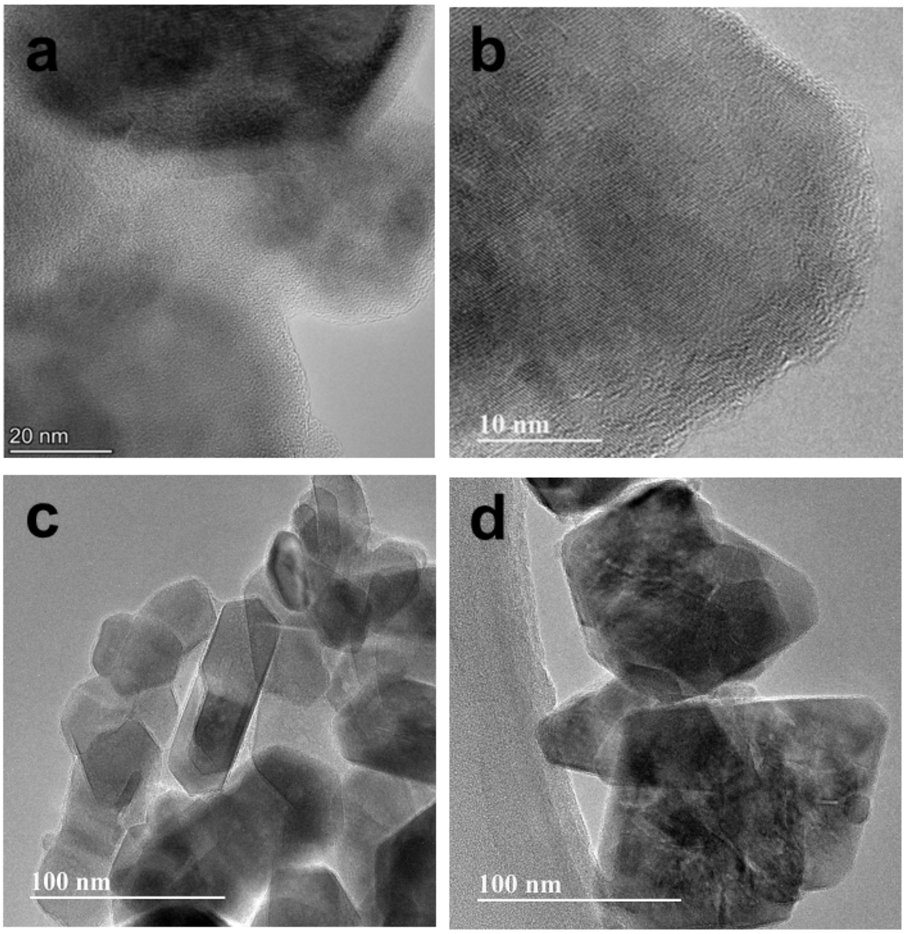

Figure S7. TEM images for FeOx catalyst.

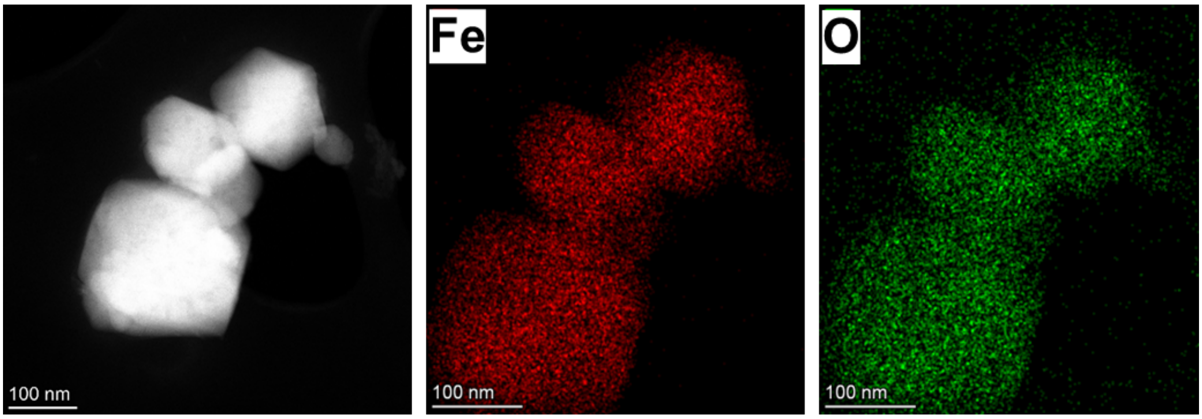

Figure S8. EDS image of FeOx.

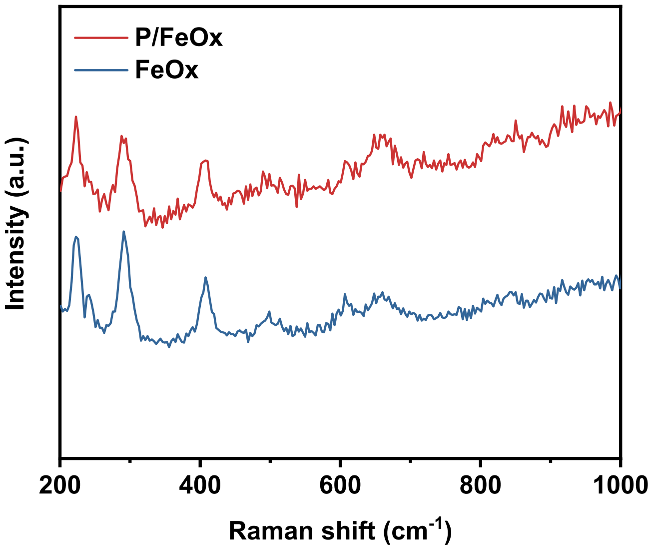

Figure S9. Raman spetrum of P/FeOx and FeOx.

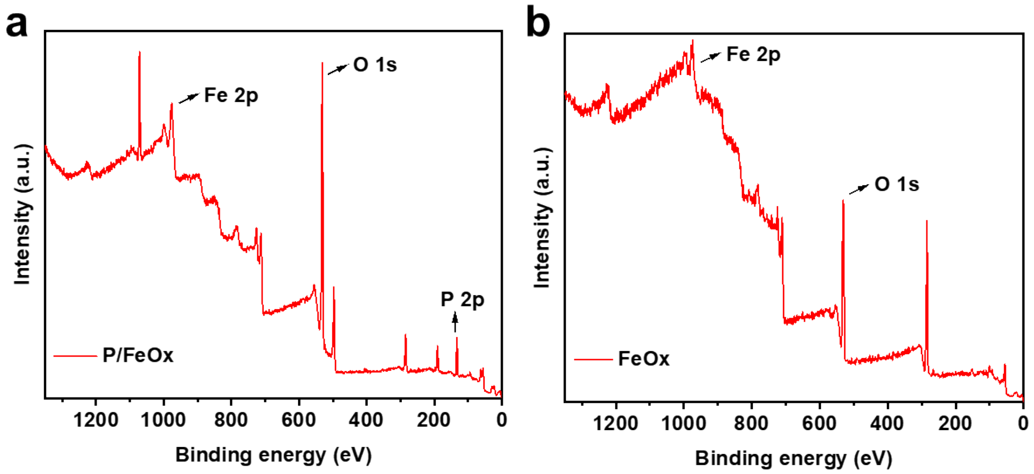

Figure S10. The XPS survey of (a) P/FeOx and (b) FeOx catalysts.

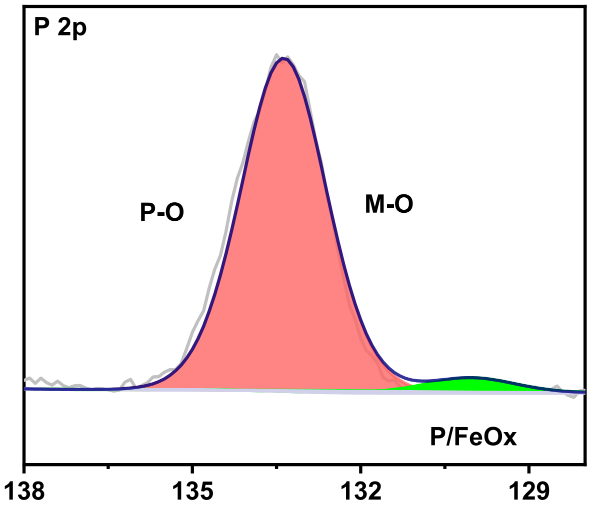

Figure S11. High resolution XPS spectra of P 2p for P/FeOx.

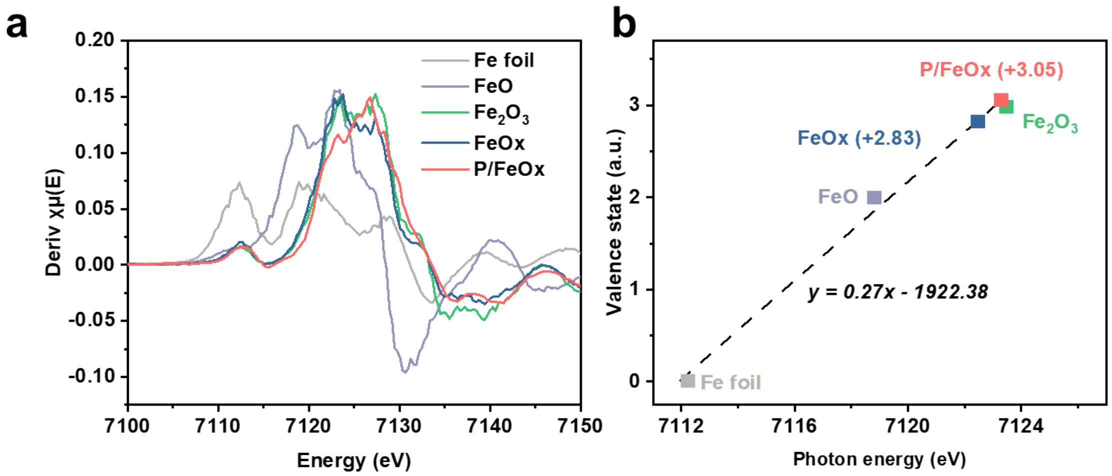

Figure S12. (a) Fe K-edge XAS derivative spectra in energy space; (b) Fe oxidation state in P/FeOx and FeOx determined from Fe K-edge XANES derivative spectra.

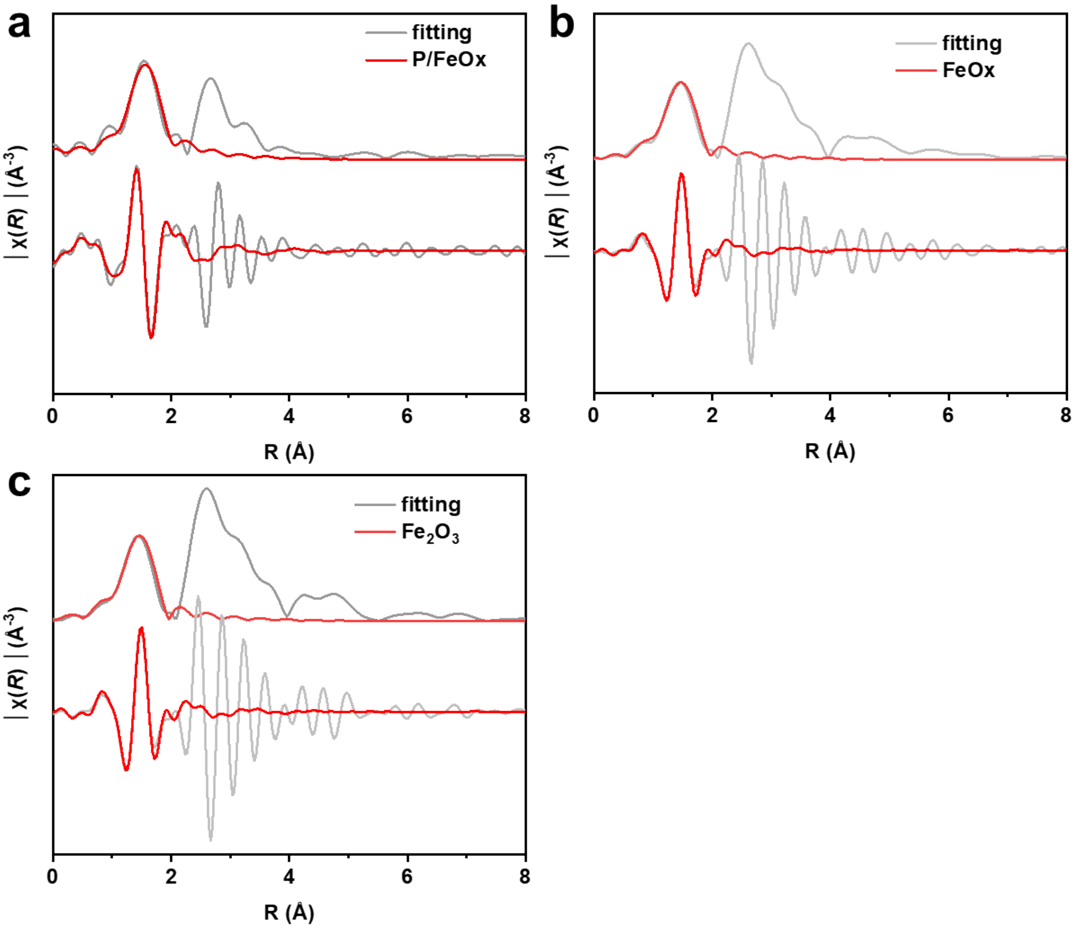

Figure S13. FT-EXAFS fitting of Fe for (a) P/FeOx, (b) FeOx and (c) Fe_2O_3 in R space.

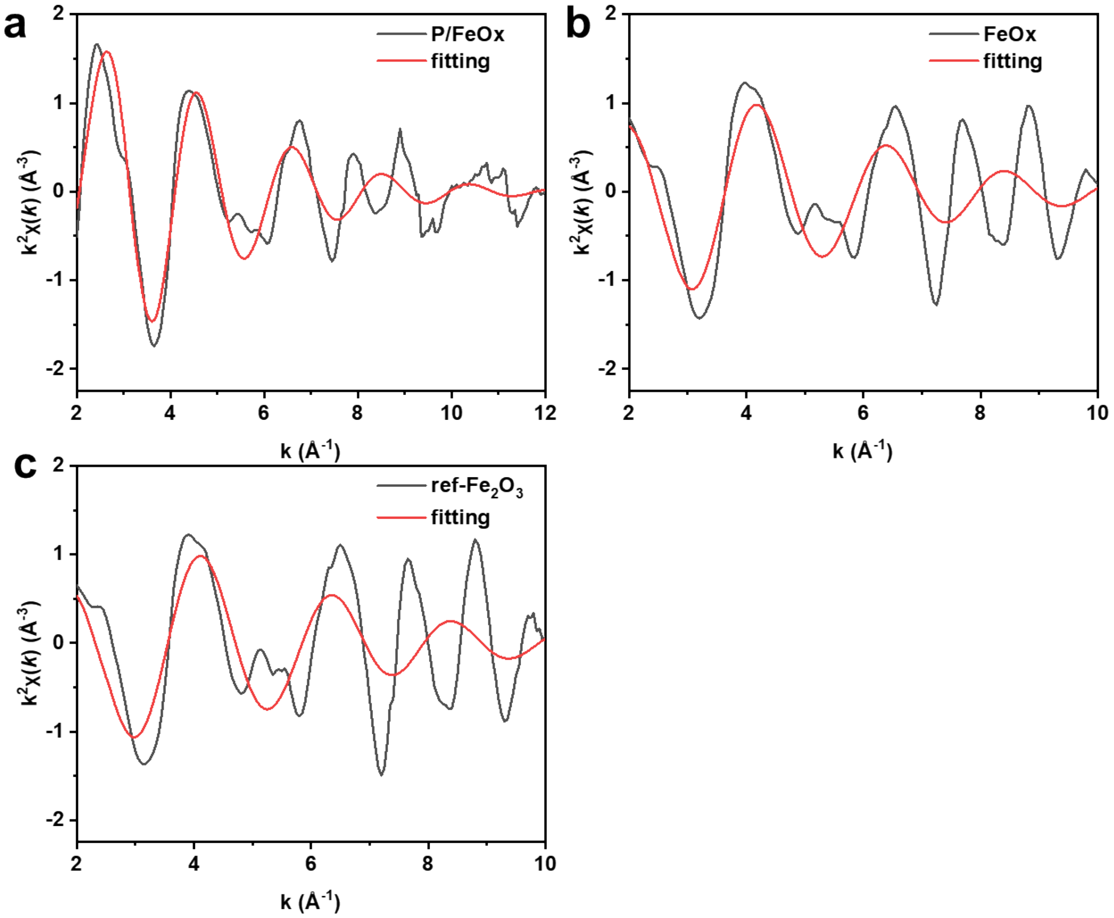

Figure S14. The corresponding FT-EXAFS k-space fitting curves of (a) P/FeOx, (b) FeOx and (c) reference Fe_2O_3 catalysts.

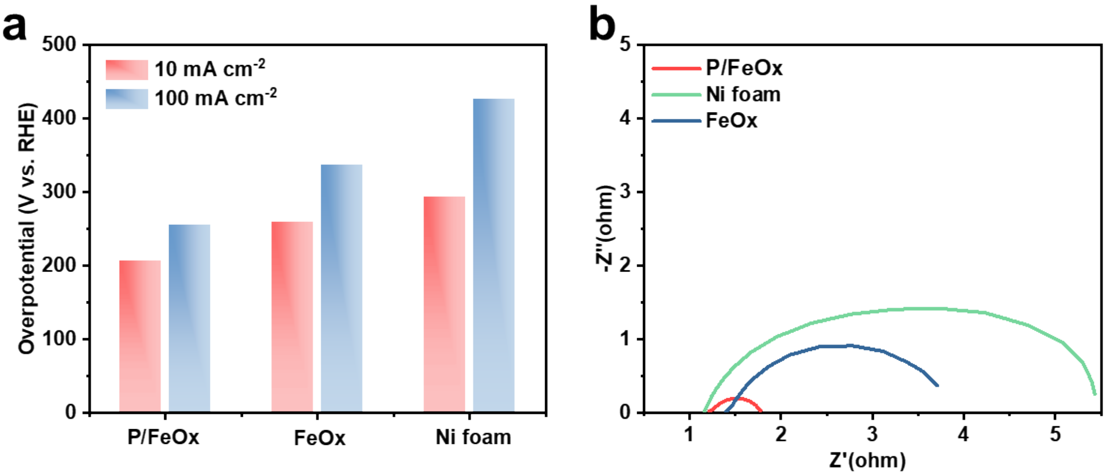

Figure S15. (a) The overpotential of different catalysts at different current densities. (b) Impedance curves of P/FeOx and its comparative samples.

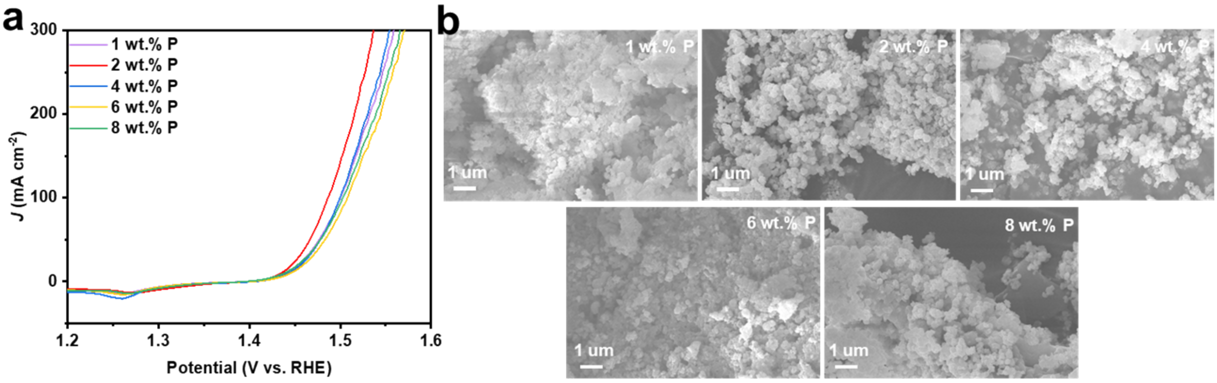

Figure S16. (a) Linear sweep voltammetry (LSV) curves and (b) SEM images of P/FeOx catalysts with different phosphorus contents (1, 2, 4, 6, and 8 wt.%) measured in 1.0 M KOH.

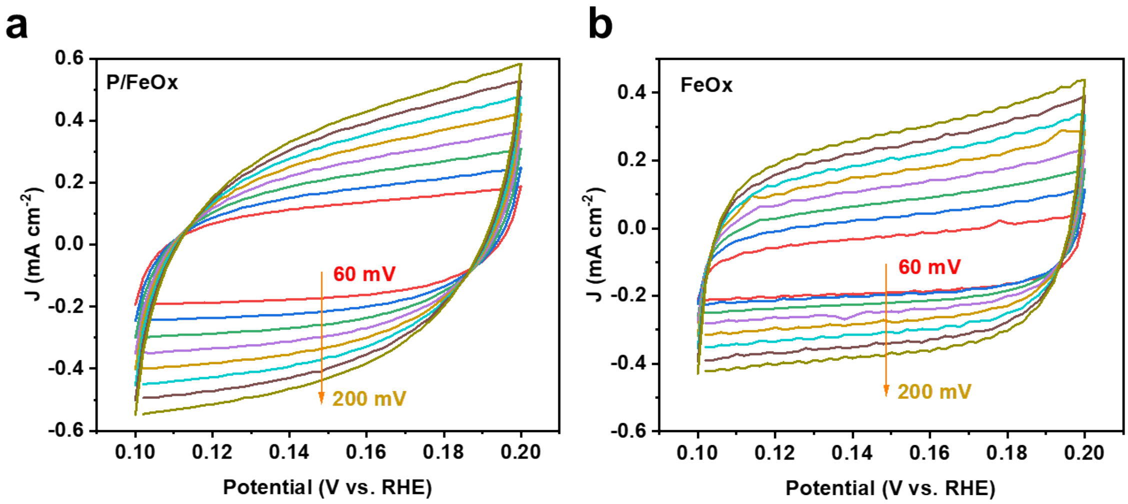

Figure S17. CV curves collected at various scan rates (60, 80, 100, 120, 140, 160, 180 and 200 mV s^{-1}) for double layer capacitance (C_{dl}) calculations of (a) P/FeOx and (b) FeOx in 1.0 M KOH.

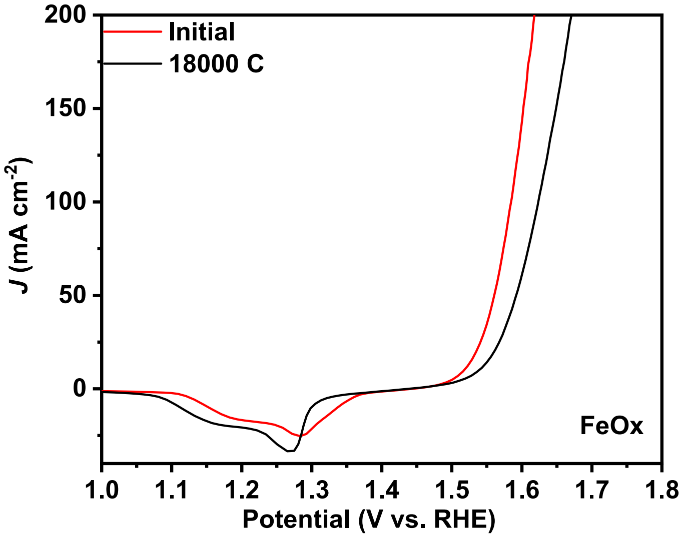

Figure S18. LSV curves for FeOx catalysts before and after 18,000 cycles in 1 M KOH.

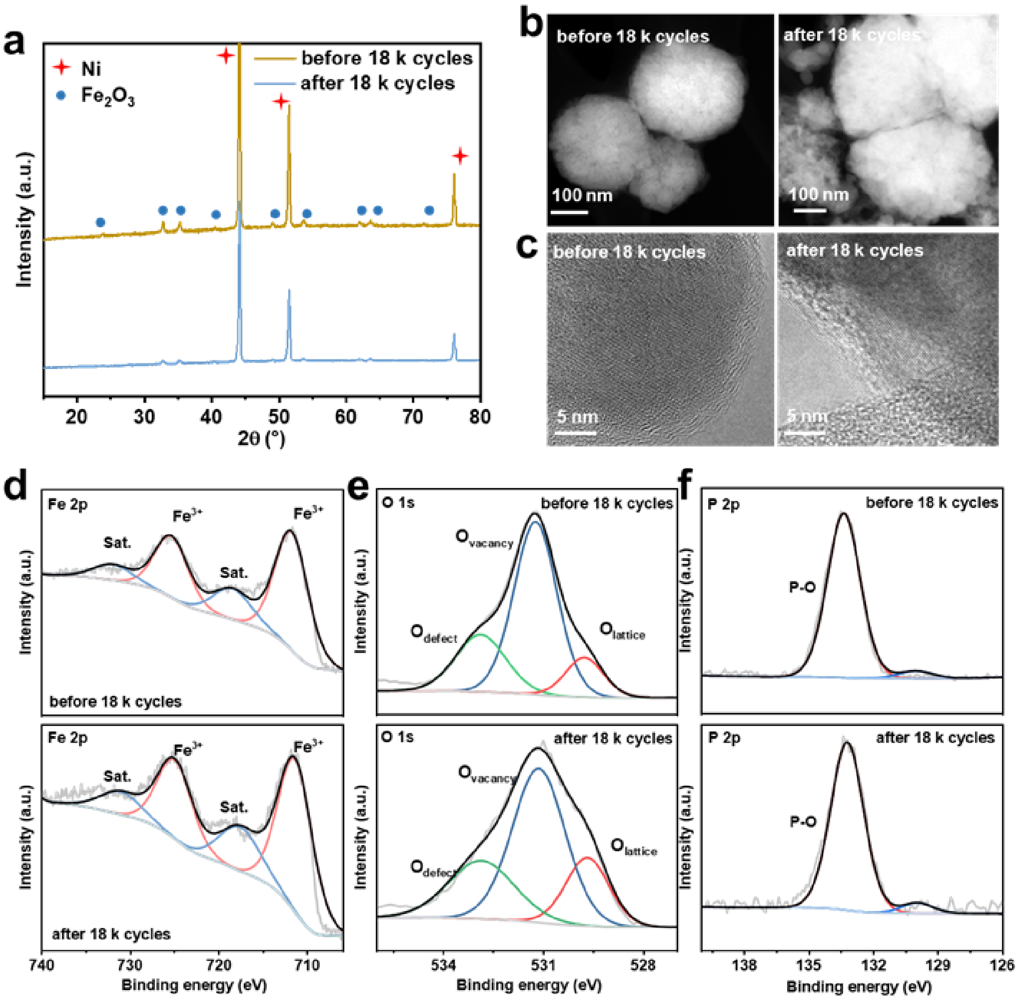

Figure S19. Characterization of P/FeOx before and after 18,000 LSV cycles. (a) XRD patterns, (b,c) STEM and TEM images, (d–f) Fe 2p, O 1s, and P 2p XPS spectra of fresh and cycled P/FeOx.

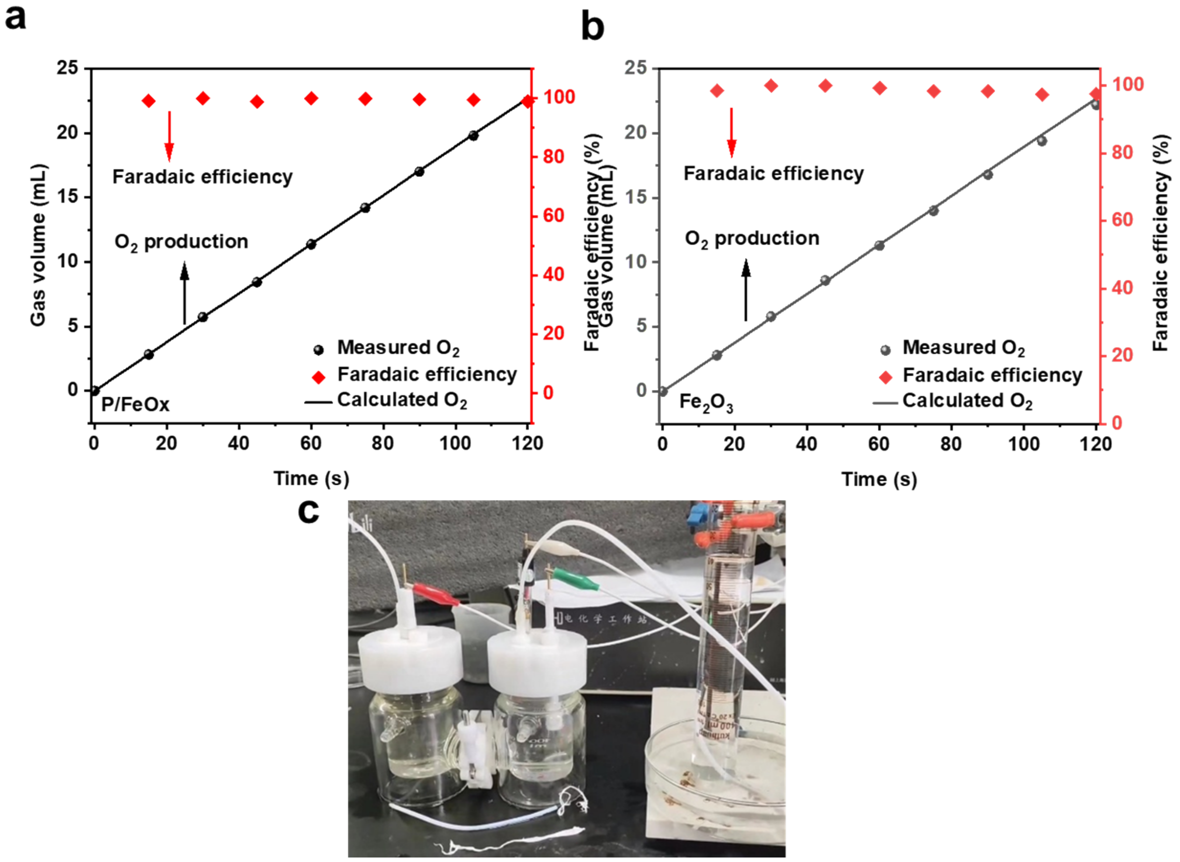

Figure S20. Faradic efficiency of (a) P/FeOx and (b) FeOx in 1.0 M KOH. (c) Schematic diagram of Faraday efficiency test.

Figure S21. Schematic illustration of AEMWEs.

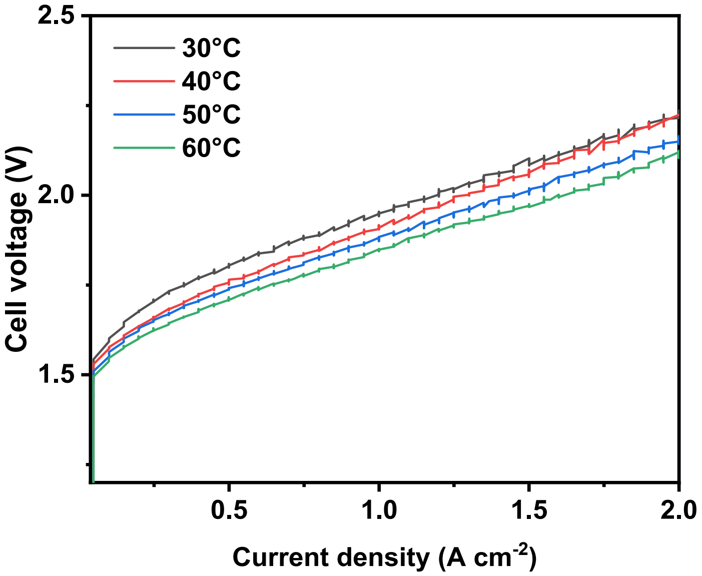

Figure S22. Polarization curves comparison of P/FeOx at different temperatures.

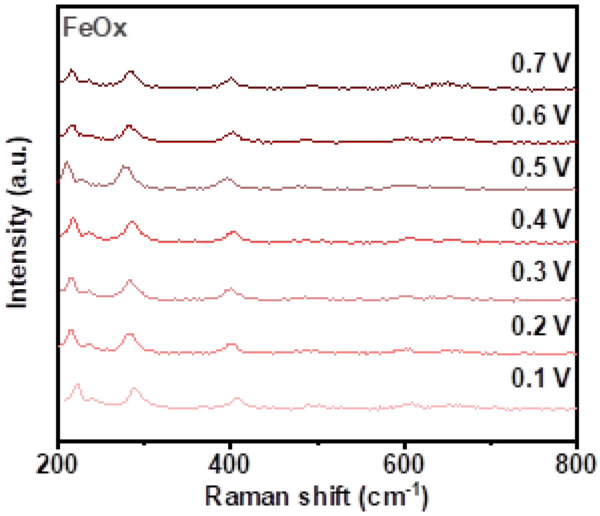

Figure S23. In situ Raman spectra of FeOx at different voltages.

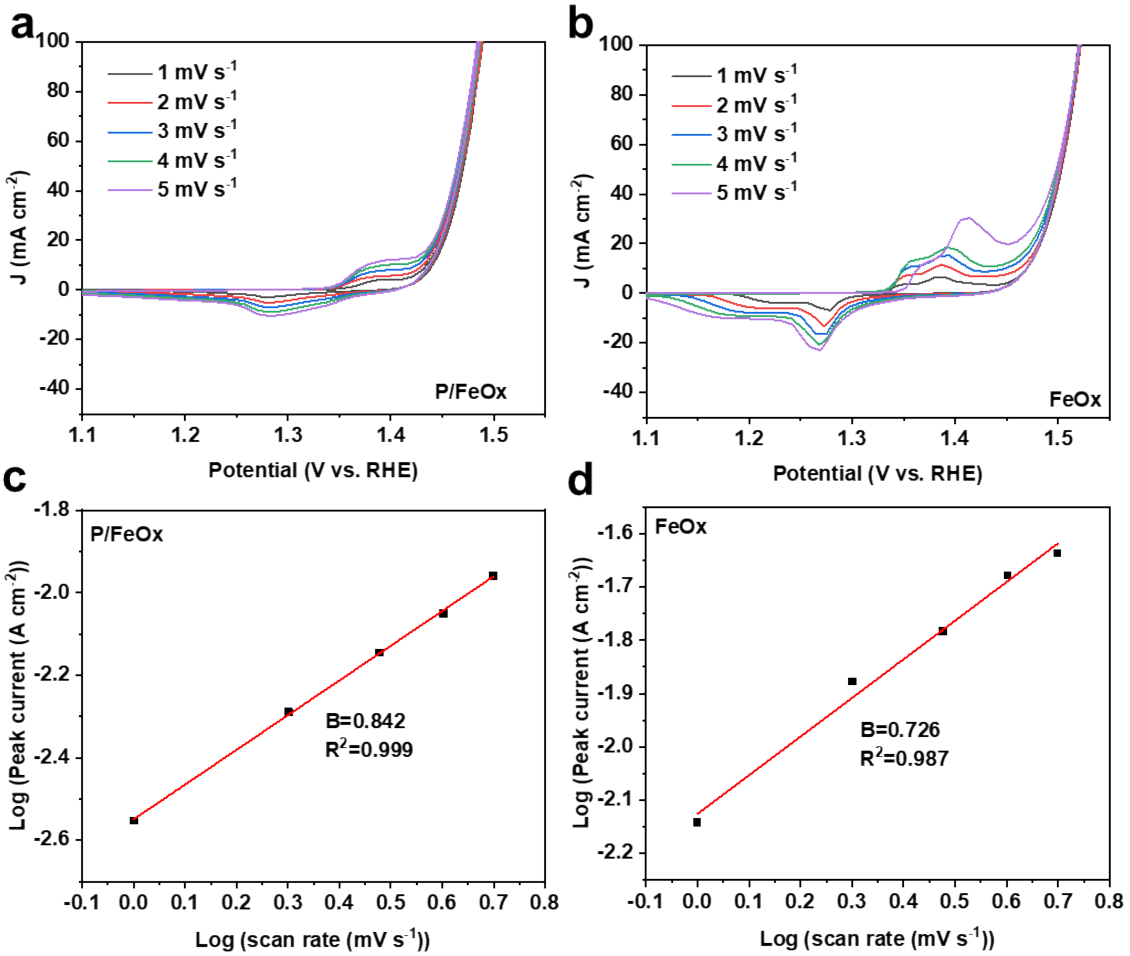

Figure S24. Calculation of contribution ratios of the capacitive and diffusion-controlled current densities: CV curves at various scan rates from 1 to 5 mV s^{-1} for (a) P/FeOx and (b) FeOx; corresponding linear-fitting calculation of b values for (c) P/FeOx and (d) FeOx

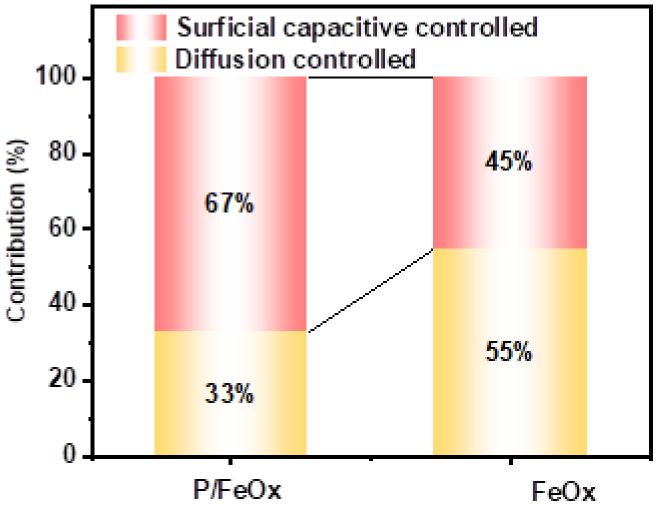

Figure S25. The contribution ratio of capacitance and diffusion control during the reaction of P/FeOx and FeOx.

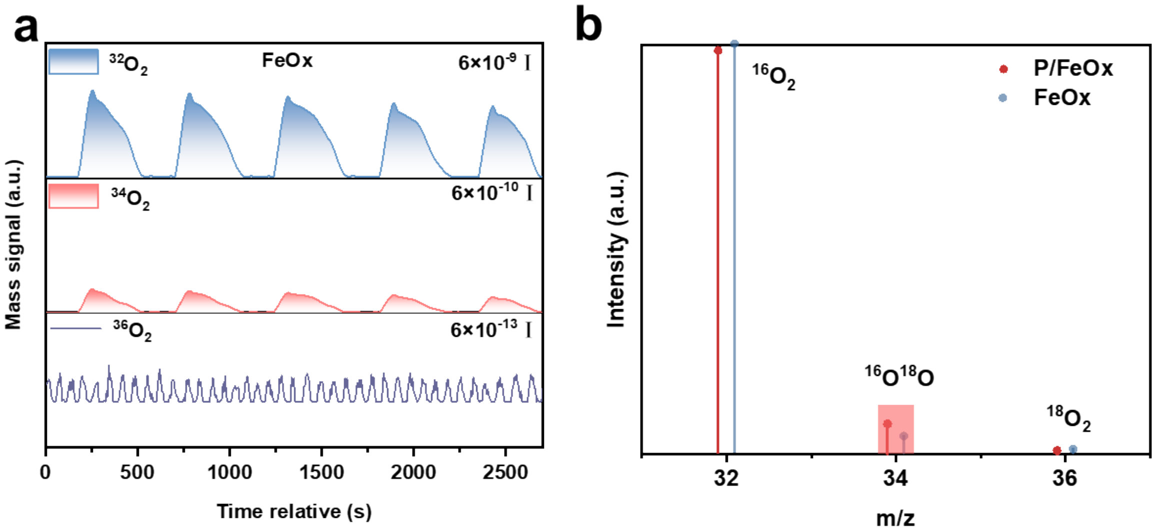

Figure S26. (a) DEMS results by ^{18}O-isotopic labeling experiments for FeOx; (b) Comparison chart of $^{16}O_2$, $^{16}O^{18}O$ and $^{18}O_2$ production of P/FeOx and FeOx during DEMS test.

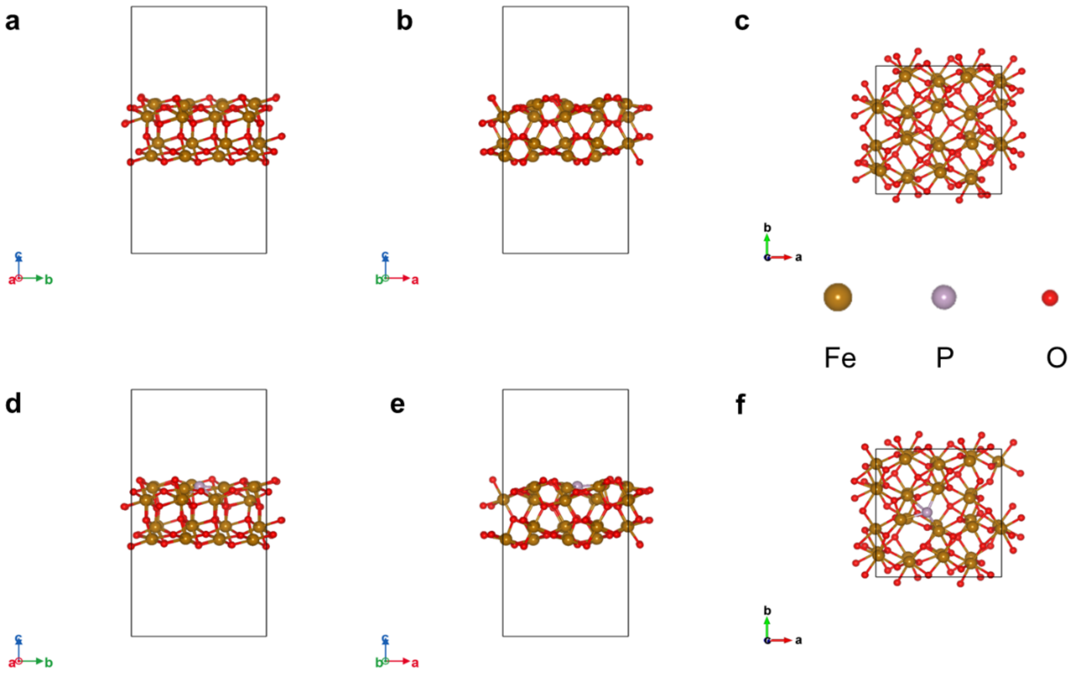

Figure S27. Optimized DFT slab models of FeOx and P/FeOx on the α-Fe_2O_3 (012) surface. (a,b) side views and (c) top view of optimized FeOx on the (012) surface. (d,e) side views and (f) top view of optimized P/FeOx on the (012) surface. Brown: Fe; red: O; purple: P.

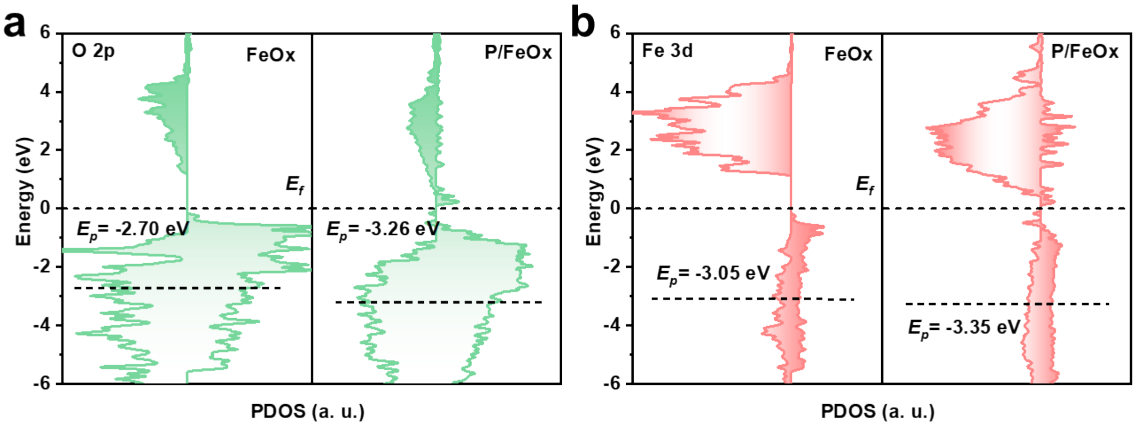

Figure S28. PDOS calculated for (a) O 2p and (b) Fe 3D in P/FeOx and FeOx.

5. Supporting Tables

Table S1. Statistical Table for P/FeOx of Element Content Analysis in EDS.

Element	Family	Atomic Fraction (%)	Atomic Error (%)	Mass Fraction (%)	Mass Error (%)	Fit error (%)
O	K	66.31	8.02	37.09	3.00	1.51
P	K	3.29	0.74	3.56	0.74	1.51
Fe	K	30.40	5.45	59.35	9.20	0.20

Table S2. Statistical Table for Element Content Analysis in XPS.

Element	Atomic percent/P/FeOx (%)	Atomic percent/FeOx (%)
Fe	3.20	2.90
O	47.64	27.54
P	6.55	/

Table S3. Fe K-edge EXAFS fitting results.

Catalyst	Path	N	R(Å)	σ^2(*10^{-3}Å)	Δ E_0(eV)	R factor (%)
P/FeOx	Fe-O	5.31	1.91	8.83	11.75	1.00
FeOx	Fe-O	5.85	1.83	8.30	-2.50	2.25
Fe_2O_3	Fe-O	6.00	1.83	7.98	-5.15	1.88

k range: 3-10.0 (Å-1); R range: 1-2 Å; S_0^2 = 0.69 was determined from the Fe foil and used for Fe K-edge fitting.

Table S4. Summary of previously reported OER catalysts with high performance.

Catalysts	Electrolyte	ŋ (mv@10 mA cm^{-2})	Ref.
This work	1.0 M KOH	208	/
P-NiMoFe-OH	1.0 M KOH	225.9	**2**
Fe-Co-P nanoboxes	1.0 M KOH	269	**3**
NiFe2O4-P	1.0 M KOH	229	**4**
Gd，Fe-NiO	1.0 M KOH	227	**5**
NiO/Co3O4	1.0 M KOH	262	**6**
Fe-NiO/NiS2	1.0 M KOH	270	**7**
Fe-NiO-Ni CHNAs	1.0 M KOH	245	**8**
Fe-Co3O4	1.0 M KOH	262	**9**
Fe-Co3O4NBs	1.0 M KOH	265	**10**
FeCoOx-Vo-S	1.0 M KOH	249	**11**
Fe-NC@CoO	1.0 M KOH	247	**12**
SnO2/MnO2	1.0 M KOH	360	**13**
Vo-Cubic-Co3O4	1.0 M KOH	375	**14**
Ni/MoOx	1.0 M KOH	333	**15**
CoFe-P	1.0 M KOH	293	**16**
FeOOH(Se)/IF	1.0 M KOH	348	**17**
P1-Co3O4	1.0 M KOH	320	**18**
1D NiFeOx-P	1.0 M KOH	237	**19**
0.01S FeOOH+1000/IF	1.0 M KOH	358	**20**

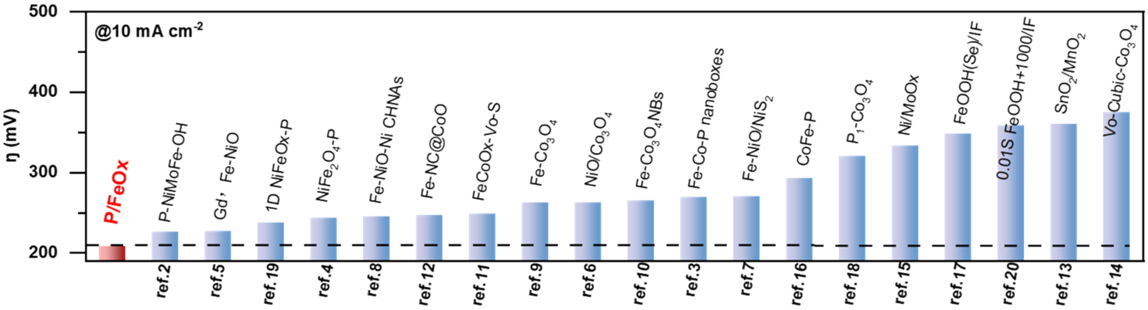

Figure S29. Overpotentials at 10 mA cm^{-2} of some recent reported articles.

Table S5. Statistical table of overpotential of catalysts with different phosphorus doping at 100 mA cm^{-2}.

Catalysts	OER-100 mA cm^{-2} (mV)
1 wt.% P	265
2 wt.% P	256
4 wt.% P	263
6 wt.% P	277
8 wt.% P	263

Table S6. Summary of previously reported AEMWE with high performance.

Catalyst	Electrolyte	Overpotential (@500 mA cm^{-2})	Current density (mA cm^{-2})	Temperature (°C)	Reference
This work	1 M KOH	1.78	500	60°C	/
NiCoP$_v$@NF	1 M KOH	1.93	500	/	[21]
P-CoVO@NF	1 M KOH	1.76	500	70°C	[22]
NiFe LDH-PMo12 // NiFe LDH	1 M KOH	1.707	200	60°C	[23]
V-NiFeOOH/Ni$_3$N	1 M KOH	1.80	587	70°C	[24]
NiCo NPs/rGO	1 M KOH	1.89	1000	60°C	[25]
NA-LT-CA	1 M KOH	1.847	500	/	[26]

References

[1]Bennett J.W., Hudson B.G., Metz I.K., Liang D., Spurgeon S., Cui Q., Mason S.E. A Systematic Determination of Hubbard U Using the Gbrv Ultrasoft Pseudopotential Set. *Comput. Mater. Sci.* **2019**, *170,* 109137.

[2] Gim, H. G.; Park, E.; Ha, J.; Lee, J.; Kim, Y. T.; Choi, J. Bifunctional Phosphorus-Doped Nimo Oxide/Ni-Fe Hydroxide Composite for Overall Water Electrolysis: Optimized Performance with Exceptional Stability. *Mater. Today Energy*, **2024**, *41*, 101526.

[3] Zhang, H.; Zhou, W.; Dong, J.; Lu, X. F.; Lou, X. W. D. Intramolecular Electronic Coupling in Porous Iron Cobalt (Oxy) Phosphide Nanoboxes Enhances the Electrocatalytic Activity for Oxygen Evolution. *Energy Environ. Sci.* **2019**, *12* (11), 3348-3355.

[4] Feng, Z.; Zhang, Z.; Zhang, X.; Li, J.; Lei, X.; Liu, X. Heating and P Doping Promote $NiFe_2O_4$ to Achieve a Faster Oxygen Evolution Reaction Pathway. *Available at SSRN 5190004*.

[5] Wang, Y.; Liu, Y.; Liu, S.; Qin, Y.; Liu, J.; Jia, X.; Jiang, Q.; Wang, X.; Zhao, Y.; Liu, L. Gd-Induced Oxygen Vacancy Creation Activates Lattice Oxygen Oxidation for Water Electrolysis. *Adv. Funct. Mater.* **2025**, 2500118.

[6] Zhang, J.; Qian, J.; Ran, J.; Xi, P.; Yang, L.; Gao, D. Engineering Lower Coordination Atoms onto NiO/Co_3O_4 Heterointerfaces for Boosting Oxygen Evolution Reactions. *ACS Catal.* **2020**, *10* (21), 12376-12384.

[7] Cheng, W.; Fan, P.; Jin, W. Visualizing the Structure and Dynamics of Transition Metal-Based Electrocatalysts Using Synchrotron X-Ray Absorption Spectroscopy. *ChemSusChem* **2025**, *18* (4), e202401306.

[8] Hu, J.; Al-Salihy, A.; Zhang, B.; Li, S.; Xu, P. Mastering the d-Band Center of Iron-Series Metal-Based Electrocatalysts for Enhanced Electrocatalytic Water Splitting. *Int. J. Mol. Sci.* **2022**, *23* (23), 15405.

[9] Chu, D.; Liang, Z.; Cheng, Y.; Chai, D. F.; Li, M. Mono-/Bimetallic Doped and Heterostructure Engineering for Electrochemical Energy Applications. *ChemSusChem* **2025**, *18* (3), e202401435.

[10] Zhao, D.; Yu, G. Q.; Xu, J.; Wu, Q.; Zhou, W.; Ning, S.; Li, X. B.; Li, L.; Wang N. Preparing Iron Oxide Clusters Surface Modified Co_3O_4 Nanoboxes by Chemical Vapor Deposition as an Efficient Electrocatalyst for Oxygen Evolution Reaction. *Energy Storage Mater.* **2024**, *66*, 103236.

[11] Yao, X.; Zhuang, L.; Jia, Y.; Liu, H.; Li, Z.; Li, M.; Zhang, L.; Wang, X.; Yang, D.; Zhu, Z. S-Modified Oxygen Vacancies in Iron-Cobalt Oxide Nanosheets: Enabling Extremely

High Activity of Oxygen Evolution Reaction for Achieving Industrial Water Splitting Benchmark. Angew. Chem. **2020**, *132* (34), 14772-14778.

[12] He, J.; Hu, Z.; Zhao, J.; Liu, P.; Lv, X.; Tian, W.; Wang, C.; Tan, S.; Ji, J. Ni-Decorated Fe-/N-Co-Doped Carbon Anchored on Porous Cobalt Oxide Nanowires Arrays for Efficient Electrocatalytic Oxygen Evolution. *Chem. Eng. Sci.* **2021**, *243*, 116774.

[13] Alwadai, N.; Manzoor, S.; Al Huwayz, M.; Abdullah, M.; Khosa, R. Y.; Aman, S.; Abid, A. G.; Alrowaili, Z.; Al-Buriahi, M.; Farid, H. M. T. Facile Synthesis of Transition Metal Oxide SnO_2/MnO_2 Hierarchical Nanostructure: As an Efficient Electrocatalyst for Robust Oxygen Evolution Reaction. *Surf. Interfaces* **2023**, *36*, 102467.

[14] Chen, X.; Xu, X.; Shao, C.; Ke, Z.; Cheng, Y.; Jin, H.; Da, Y.; Liu, D.; Chen, W. Facet-Dependent Lattice Oxygen Activation on Oxygen-Defective Co_3O_4 for Electrocatalytic Oxygen Evolution Reaction. *ACS Energy Lett.* **2024**, *9* (5), 2182-2192.

[15] Ni, S.; Qu, H.; Xing, H.; Xu, Z.; Zhu, X.; Yuan, M.; Wang, L.; Yu, J.; Li, Y.; Yang, L. Donor-Acceptor Couples of Metal and Metal Oxides with Enriched Ni^{3+} Active Sites for Oxygen Evolution. *ACS Appl. Mater. Interfaces* **2021**, *13* (15), 17501-17510.

[16] Li, P.; Li, W.; Chen, R.; Lin, Y. Boosting the Oxygen Evolution Electrocatalysis Performance of Iron Phosphide via Architectural Design and Electronic Modulation. *ACS Sustainable Chem. Eng.* **2020**, *8* (24), 9206-9216.

[17] Niu, S.; Jiang, W. J.; Wei, Z.; Tang, T.; Ma, J.; Hu, J. S.; Wan, L. J. Se-Doping Activates FeOOH for Cost-Effective and Efficient Electrochemical Water Oxidation. *J. Am. Chem. Soc.* **2019**, *141* (17), 7005-7013.

[18] Zhou, X.; Liao, X.; Pan, X.; Yan, M.; He, L.; Wu, P.; Zhao, Y.; Luo, W.; Mai, L. Unveiling the Role of Surface P–O Group in P-Doped Co_3O_4 for Electrocatalytic Oxygen Evolution by on-Chip Micro-Device. *Nano Energy* **2021**, *83*, 105748.

[19] Li, X.; Deng, C.; Kong, Y.; Huo, Q.; Mi, L.; Sun, J.; Cao, J.; Shao, J.; Chen, X.; Zhou, W. Unlocking the Transition of Electrochemical Water Oxidation Mechanism Induced by Heteroatom Doping. *Angew. Chem. Int. Ed.* **2023**, *62* (40), e202309732.

[20] Zhang, X. Y.; Li, F. T.; Dong, Y. W.; Dong, B.; Dai, F. N.; Liu, C. G.; Chai, Y. M. Dynamic Anion Regulation to Construct S-Doped Feooh Realizing 1000 mA cm^{-2}-Level-Current-Density Oxygen Evolution over 1000 h. *App. Catal. B: Environ.* **2022**, *315*, 121571.

[21] Guo, L.; Chi, J.; Cui, T.; Zhu, J.; Xia, Y.; Guo, H.; Lai, J.; Wang, L. Phosphorus Defect Mediated Electron Redistribution to Boost Anion Exchange Membrane-Based Alkaline Seawater Electrolysis. *Adv. Energy Mater.* **2024**, *14* (31), 2400975.

[22] Liang, Z.; Shen, D.; Wei, Y.; Sun, F.; Xie, Y.; Wang, L.; Fu, H. Modulating the Electronic Structure of Cobalt-Vanadium Bimetal Catalysts for High-Stable Anion Exchange Membrane Water Electrolyzer. *Adv. Mater*. **2024**, *36* (41), 2408634.

[23] Cai, Z.; Wang, P.; Zhang, J.; Chen, A.; Zhang, J.; Yan, Y.; Wang, X. Reinforced Layered Double Hydroxide Oxygen-Evolution Electrocatalysts: A Polyoxometallic Acid Wet-Etching Approach and Synergistic Mechanism. *Adv. Mater.* **2022**, *34* (26), 2110696.

[24] Thangavel, P.; Lee, H.; Kong, T. H.; Kwon, S.; Tayyebi, A.; Lee, J. h.; Choi, S. M.; Kwon, Y. Immobilizing Low-Cost Metal Nitrides in Electrochemically Reconstructed Platinum Group Metal (Pgm)-Free Oxy-(Hydroxides) Surface for Exceptional OER Kinetics in Anion Exchange Membrane Water Electrolysis. *Adv. Energy Mater.* **2023**, *13* (6), 2203401.

[25] Tian, C.; Liu, R.; Lv, Z.; Wang, C.; Liu, W.; Dong, F.; Feng, X.; Yang, W.; Wang, B. Heterogeneous Support Effects for Enhanced Performance in Anion Exchange Membrane Water Electrolysis. *Adv. Energy Mater.* **2025**, *15* (36), e01952.

[26] Jiang, X.; Kyriakou, V.; Wang, B.; Deng, S.; Costil, S.; Chen, C.; Liu, T.; Deng, C.; Liao, H.; Jiang, T. Hierarchical Microporous Ni-Based Electrodes Enable “Two Birds with One Stone” in Highly Efficient and Robust Anion Exchange Membrane Water Electrolysis (AEMWE). *Chem. Eng. J.* **2024**, *486*, 150180.